Comparing Isotropic and Anisotropic Brain Conductivity Modeling: Planning Optimal Depth-Electrode Placement in White Matter for Direct Stimulation Therapy in an Epileptic Circuit

Leopoldo Cendejas Zaragoza[1], Brian Hondorp[2], and Marvin A. Rossi[*3]
[1]ITESM CCM, Mexico City, Mexico, [2]Rush Medical College, Chicago, IL, [3]Rush University Medical Center, Chicago, IL
*Corresponding author: 1725 W. Harrison St. Suite 885, Chicago, IL, marossi@usa.net

Abstract: A novel depth electrode placement planning strategy is presented for calculating a patient-specific brain conductivity map for predicting the extent to which direct stimulation therapy can strategically propagate through pathological white matter. Our laboratory developed isotropic and anisotropic human brain finite element method (FEM) models derived from magnetic resonance imaging (MRI) and diffusion tensor imaging (DTI), respectively, for estimating tissue conductivities during direct stimulation therapy. Specifically, the electro-static electric field (E-field) and, current density surrounding two modeled depth contacts virtually placed in white matter were modeled for a patient with bilaterally independent intractable temporal lobe epileptic sources. The more sophisticated anisotropic model was developed to challenge our three-compartment isotropic model (Rossi et al, 2010). The isotropic model was used to plan optimal implantation of a 4-contact depth lead connected to an investigational implantable pulse generator (NeuroPace®, Inc) recently recommended for approval by the U.S. Food and Drug Administration.

Keywords: deep brain stimulation, brain computer interface, tractography, refractory epilepsy, neural prosthesis.

1. Introduction

Responsive neurostimulation (RNS™ System, NeuroPace®, Inc. Mountain View, CA) is an investigational technology recently unanimously recommended for approval by the Food and Drug Administration (FDA) as adjunctive therapy in individuals with pharmacologically resistant focal-onset epilepsy. Efficacy of the NeuroPace® RNS™ System was assessed in a multi-center pivotal clinical trial (Morrell et al, 2008; 2009). This technology capitalizes on a closed-loop approach. That is, delivery of direct stimulation is contingent upon detecting the electrographic seizure onset. The stimulation parameters used by the implantable pulse generator (IPG) has been reached by trial-and-error. The neurostimulation paradigm for the RNS™ System was initially taken from afterdischarge study paradigms (Lesser et al., 1999).

A critical first step toward effectively applying direct brain stimulation therapy in epilepsy is to interface with epileptic neural tissue. Epileptogenic cortex can include pathways that connect distant modulatory territories such as thalamus and pathological cortical regions (Luders et al., 2004). The term, 'epileptic focus' becomes a misnomer when such epileptic circuits are discussed. What remains unclear is how local stimulation can modulate potentially distant communicating epileptic tissue that may involve both cortical and subcortical regions.

Proposed mechanisms explaining acute-onset efficacy of local neurostimulation therapy include, conduction blockade (Beurrier et al., 2001), synaptic inhibition (Dostrovksy et al., 2000), synaptic depression (Urbano et al., 2002), and overriding pathophysiological neural network activity (Montgomery and Baker, 2000; Fukuda et al, 2001; McIntyre et al., 2004; Zumsteg et al, 2006). In addition, chronic exposure to direct neurostimulation has been associated with distant cortical synaptic proliferation (Keller et al, 1992).

Conversely, the possibility of enhancing pathological synaptic transmission cannot be ignored. Direct neurostimulation can acutely provoke the already hyperexcitable neural network. Moreover, well-established animal models demonstrate that chronic local delivery of specific stimulation parameters can produce secondary epileptogenesis (McIntyre & Goddard, 1973; VanLandingham & Lothman, 1991). Therefore, a substantial range of factors must be considered in the clinical response to stimulation delivered directly to neuronal populations. These

variables include the number and inter-dependence of anatomical targets, electrode number, electrode location and orientation, geometry or shape of the electrode contacts, stimulation parameter settings (Butson et al., 2007), distribution of cathode and anode (Durand & Bikson, 2004), and the biophysical properties of stimulated medium compartments.

The goal of the depth electrode placement planning workflow developed in this study is to establish the feasibility of predicting with individual specificity, distant activation sites within the epileptic circuit communicating via white matter tracts. We hypothesize that it is possible to control the extent of neural tissue influenced in the mesial temporal regions by interfacing strategically placed depth leads for delivering direct neurostimulation therapy.

Recently published data reveal that therapeutic direct stimulation in mesial temporal epilepsy consistently target hippocampal grey matter regardless of surrounding sclerosis (Velasco et al, 2000; 2001; Vonck et al, 2002; Boon et al, 2007). An alternative approach is lead placement at the grey-white junction to allow the same depth lead to deliver therapeutic current to white matter propagation pathways while detecting the ictal onset in grey matter.

Our center has successfully implanted investigational RNS™ System depth electrodes in juxtacortical epileptic mesial temporal white matter since 2004. Parahippocampal white matter has robust afferent and efferent hippocampal pathways (Lavenex et al, 2007). Our goal has been to enhance propagation to distant epileptic tissue through white matter tracts. Achieving such activation using two four contact RNS™ System leads may be improved with patient-specific placement planning. A presurgical workflow has evolved from this experience at Rush University Medical Center (RUMC) with the objective of maximally activating the epileptic network with therapeutic stimulation.

2. METHODS

Two techniques are described in this study and treated individually as computationally-intensive modules. The first module was employed prior to depth lead implantation. The initial module employed isotropic finite element method (FEM) modeling to predict the maximal E-field magnitude immediately surrounding active cylindrical depth contacts. The volume of cortical activation (VOCA) was calculated from the greatest magnitude of the electric field immediately surrounding the active contacts. The VOCA as used in this study targeted the grey white white matter junction. As a first approximation, we assumed constant and uniform bulk conductivities for isotropic white and grey matter, and cerebrospinal fluid (CSF) compartments.

Anisotropic modeling of the VOCA was performed post-implantation to challenge our presurgical isotropic planning model. We implemented this module following implantation of the depth leads due to a time lag required for evolving CPU power and software platforms required to manage our data-intensive processing.

The post-implant validation module is descriptively named subtracted activated SPECT (SAS). SAS captured transient blood flow changes during delivery of direct stimulation as an indirect measure of focal neural activation (Rossi et al, 2008; Rossi et al, 2010). This strategy was essential for validating the predicted white matter-connected circuit actually activated by the given stimulation parameters, electrode location and lead orientation. In order to prevent unintended outcome biases, SAS post-acquisition processing was completed after completing our anisotropic modeling analyses.

2.1. Subject

Our subject was a 38 year old female at the time of her presurgical evaluation. She has a long-standing history of refractory temporal lobe seizures since childhood. Video-EEG monitoring revealed a prominent symptomatogenic epileptic region in both temporal regions clinically associated with an alteration in awareness and lip smacking. Electrographically, a build up and evolution of right anterior temporal rhythmical theta range activity was correlated with the semiology. No prior intracranial electro-corticography (ECoG) recording was performed. Since this individual had active bilateral independent temporal lobe epileptic sources, she was not a candidate for epilepsy resective surgery, but qualified for the RNS™ System Pivotal Clinical Trial prior to it closing in 2010. The protocol described herein, and the multi-center RNS™ System Pivotal Clinical Trial were

both approved by the RUMC Institutional Review Board. Our subject voluntarily enrolled in both studies.

2.2. Diffusion Tensor Imaging (DTI)

DTI sequences were acquired as diffusion weighted single shot spin echo. Echo planar images were axially acquired with the following parameters: TR/TE=12100/97 ms, field of view=25 cm, matrix=128×128, 38 3 mm gapless slices, 6 repetitions, in plane resolution=1.95 mm. Two diffusion weights (b-values) were used: b=0 and b=800 s/mm^2. The high b-value was obtained by applying diffusion encoding gradients along 24 non-collinear directions. This acquisition scheme was repeated six times for each slice, with the sign of all the gradient directions inverted for every other repetition. This acquisition scheme overcomes the inherent variance of DTI acquisitions during the scanning session. An additional set of inversion recovery images with cerebrospinal fluid nulling (TI ~ 2100 ms) was acquired for each slice with b=0 s/mm^2. These images were used to un-warp the eddy current effect of the diffusion gradients (de Crespigny et al., 1998).

A structural 3D Fourier transform spoiled gradient recalled (SPGR) MR sequence (124 axially acquired 1.6 mm slices, 256 mm x 256 mm field of view and 0.85937 mm^3 isotropic voxels) was acquired for the same patient.

2.3. Pre-implant Isotropic VOCA Modeling

Predicting the VOCA directly surrounding RNS cylindrical depth electrode contacts was calculated presurgically in anticipation of stereotactically placing the lead in left basal temporal white matter of our subject. This first approximation assumed that each material or tissue was a homogenous and isotropic medium.

Preprocessing of the neuroimaging data was performed in a series of steps which convert SPGR gapless MRI sequences into a variable density mesh upon which simulation parameters are applied. This process is initiated by processing raw MRI data with the Seg3D (University of Utah) software package. Pre-processing was performed to minimize segmentation compartment artifacts with an intensity correction filter that suppresses low frequency background non-uniformities. Manual skull extraction was performed by masking non-brain tissue. A finite element brain mesh was generated from this dataset using ScanIP (v5.1, Simpleware, LTD). The isotropic brain model was modeled as three compartments (grey and white matter) with uniform conductivity (Figure 1).

The anterior tip of the electrode lead was located at the amygdala-hippocampal border. These electrode coordinates were manually integrated with the generated brain by one of the co-authors (MAR), a board certified epilepsy neurologist. A CAD model of the depth electrode model was manually and interactively positioned in the left and right temporal white matter within 4-5 mm of the white-grey matter interface using Simpleware +CAD module (Figure 2). The depth lead was modeled according to the specifications of the actual electrode lead used in the RNS^{TM} pivotal clinical trial. Specifically, the CAD model consisted of four conductive cylinders (1.27 mm diameter x 2 mm height) separated by insulators (10 mm between the midpoints of the conducting cylinders). The resultant composite of brain and CAD electrode were used to generate a multipart volumetric mesh using the ScanIP software package FE+ free-meshing algorithm (Simpleware, LTD). Mesh density was designated by specifying the maximum edge length of a mesh component tetrahedron.

To maximize computing efficiency, a variable mesh density was employed, with a maximum edge length of 0.25 mm lying within 40 mm of each electrode contact, transitioning linearly to a maximum edge length of 5 mm over a transition radius between 40 mm and 100 mm. At greater than 100 mm the maximum edge length for mesh tetrahedral components was 5 mm. These mesh data were imported into COMSOL to define the model geometry. This composite model was generated using approximately 235,000 geometry elements.

2.4 Anisotropic VOCA Modeling

COMSOL processing limitations, constrained the computationally-intensive anisotropic model to single slice 2D representations. The anisotropic model was determined from 8100 contiguous transformed matrices within a brain slice of a high-resolution DTI dataset acquired 30-45 minutes following a complex partial seizure without generalization secondarily. Each 3x3 tensor matrix composing a voxel represented acute and transient water diffusion-related changes occurring after the focal seizure. A

custom program was developed in MATLAB v2008b to convert each *diffusion tensor matrix* in an axial brain slice to a *conductivity tensor matrix* using a linear transformation of the matrices' eigenvalues (Tuch et al, 2001). A rectangular geometric entity was created for each voxel, positioned at its proper spatial coordinate, and related to the corresponding conductivity tensor using the LiveLink-for-MATLAB module to COMSOL interface.

A 2D electrode model was included within the created anisotropic brain tissue geometry, this electrode model was generated with respect to the trial RNS electrode as follows: A 2D slice of the electrode was represented as four conductor rectangles (1.27mm height x 2mm base) separated by insulators (10 mm between mid-points of the conductors).

The anterior electrode lead was positioned at the amygdala-hippocampal border just as in the isotropic model. Meshing process was performed in COMSOL. A free triangular mesh was chosen, defining a finer mesh size surrounding the electrode geometric domains. The complete mesh consisted of 42,796 domain elements with 18,180 boundary elements.

Data processing was performed on a Windows 7 based 64-bit dual 8-core (32 virtual cores) workstation with 192 GB usable RAM. The Poisson equation solved with an efficient Fourier FEM solver (UMFPACK) within COMSOL was employed to model the electric field generated during bipolar stimulation of the two anterior depth contacts for each electrode. A stimulation current of 4.5 mA across a 500 Ohm load-resistance was converted to a 5 V peak-to-peak potential difference. This voltage conversion was within a therapeutic range used for those subjects implanted with at least one RNS™ System depth lead with mesial temporal epileptic sources (Morrell, 2008). These settings generated a calculated charge density = 9.1 $\mu C/cm^2$ delivered to the two cylindrical electrode contacts with opposite polarities. For simplicity, time dependence was omitted from the calculations. The measured potential difference was used as an electrostatic scalar V to calculate the electric field (E) in a homogeneous isotropic medium, where, E = -gradient(V).

The isotropic spherical VOCA solution as derived from the maximum electric field magnitude was used to seed the patient's DTI for anticipated placement of the depth lead contacts. Expected white matter bundles recruited were modeled by diffusion tensor tractography using these seed regions of interest (ROI). The active bundles were estimated by examining the principal diffusion direction of adjacent voxels using a deterministic tracking algorithm from a continuous tensor field of the tensor elements (MR VISTA; http://white.stanford.edu/software).

2.5. Post-Implant Validation by Subtracted Activated SPECT

The final SAS module of the workflow was used to validate the presurgically modeled VOCA and white matter propagation circuit. This process was implemented 8 months following stereotactic implantation of the depth leads longitudinally in temporal white matter bilaterally. The same implanted contacts were used for both eCoG recording and delivering stimulation therapy. The IPG can was implanted in the skull.

The stimulation parameters used in the presurgical simulation were actually delivered during post-implantation testing through posterior depth contacts 3-4 in a bipolar configuration while capturing resulting transient blood flow changes. The peripheral intravenous injection of a 5 cc bolus of ^{99m}Tc-HMPAO was completed during delivery of six high frequency stimuli (200 Hz) at approximately 2 second intervals.

The activated SPECT dataset was normalized and subtracted from a baseline SPECT using a relative subtraction technique developed in collaboration with BluePointDX (Antrim, NH), RUMC, and Samsung-NeuroLogica Corp (Danvers, MA) (Rossi & Krug, 2012). The RNS™ depth leads did not capture seizures for 24 hrs prior to acquisition of the baseline SPECT. The SAS, post-implant CT (1 mm slice thickness, 168 contiguous axially acquired slices on a GE LightSpeedR scanner), and SPGR MR datasets were co-registered using MIM (Cleveland, OH).

3. RESULTS

3.1. Pre-implant Isotropic E-Field Modeling

A first approximation of predicting the stimulation-related VOCA was performed in a model of three homogeneous isotropic media representing white matter, grey matter, and cerebrospinal fluid. The 3D and 2D isotropic models

representing the uniform E-field are shown in Figure 3. Post-processing of the E-field solution was visualized in COMSOL as a 3D isosurface plot. The electric field strength within the modeled VOCA was measured along a transept line placed radially through the electrode contact center (Figure 4).

A VOCA of 220 mm^3 was calculated surrounding each of the two active cylindrical electrode contacts defining the maximal electric field strength of 900-1000 V/m expected to activate neuronal axons. This force estimate was taken from previously published data of neuronal activation cable models (Butson & McIntyre, 2005; 2006; Butson et al, 2007). This assumption was used as a first approximation to understand if this field strength estimate from the published literature could be extrapolated to model activation of axonal pathways of a cortical neuronal circuit. As expected, the strength of the modeled electric field decreased inversely proportional to the square of the field's radius. The maximal field strength of 900-1000 V/m resulted in the electric field's maximal magnitude radius of 3.75 mm from shaft center (3.12 mm from electrode surface; see Figure 4B). A distance of 5 mm from the grey matter boundary was beyond the reach of the electric field's neural activation radius. Therefore, the boundary of the electric field's maximal magnitude overlapping the VOCA was assumed to remain in white matter with a constant conductivity. The electric field did not extend to grey matter where the change in conductivity would have deformed the spherical electric field volume. For simplicity, in-homogeneities of the fringe field at the edges of the electrode contacts were not considered.

This VOCA spherical isotropic model surrounding 4 modeled cylindrical electrode contacts of the depth lead was positioned within the DTI representing white matter 5 mm lateral to the left hippocampal formation. The model was within our DTI voxel resolution of 1.95 x 1.95 x 3 mm^3. The spherical model was placed in left paramesial temporal lobe white matter (Figure 5). The depth lead model was oriented longitudinally in inferior temporal lobe white matter that included the parahippocampal region. The calculated tractography model simulated the extent of white matter trajectories activated during delivery of direct stimulation via a depth electrode. These white matter pathways included: 1) ipsilateral (left) optic radiation tracts projecting to the left occipital lobe, 2) a projection to the ipsilateral thalamus, 3) a temporofrontal pathway ending in the ipsilateral basal frontopolar region, and 4) the contralateral posterior superior temporal gyrus confluent with the posterior corpus callosum (Figure 5B).

Stereotactic implantation of the depth lead was completed using a posterior-to-frontal longitudinal approach in paramesial white matter in both temporal lobes. This trajectory was guided by our pre-implantation depth lead planning model. An occipital approach was facilitated by a Stealth^{TM} (Medtronic, Inc) MRI navigational system (Figure 6). These same implanted contacts were used for both eCoG recording and delivering stimulation therapy. The neurostimulator generator was implanted in the skull.

3.2. Post-implantation Anisotropic Modeling

The anisotropic associated E-field and current densities followed anatomical boundaries not apparent in the isotropic conductivity model. The anisotropic modeled 2D E-field and current density maps generated in a single slice are shown in Figures 7B & C.

3.3. Post-Implant Validation

A SAS study acquired during stimulation of posterior depth contacts 3-4 demonstrated transient hypoperfusion-related changes beyond the neural tissue immediately surrounding the stimulated depth electrode contacts. No after-discharge was recorded at the site of stimulation as recorded by ECoG. Therefore, these transient hypoperfusion-related changes were due to direct stimulation itself and not by epileptiform activity or a seizure. These data suggest communication of the white matter within the VOCA surrounding the depth electrode with ipsilateral occipital and frontal cortices, as well as contralateral neocortical temporal grey matter. (Figure 8). Connectivity of the visualized SAS regions representing blood flow demand mediated by adjacent grey matter were clearly bridged by the pre-implant tractography map.

4. DISCUSSION

We used a novel computationally intensive approach to predict targeted propagation of electrical current, prior to stereotactically placing

an RNS™ System depth lead at the grey-white matter junction in epileptic temporal white matter. Preoperatively, using an isotropic model, the maximal E-field gradient surrounding the active electrode contacts provided an estimate of the extent of cortical activation modeled during bipolar stimulation. Anisotropic modeling demonstrated changes in the electric field distribution due to the heterogeneous conductivities. Furthermore, the simulation suggested that current tends to flow according to directionality in a conductivity tensor field.

The anisotropic study takes into consideration the difference in conductivity between one voxel and another, rather than identifying uniform conductivity changes limited to three brain compartments as considered in the isotropic model. This means that each considered voxel has its own conductivity relationship obtained from the DTI dataset.

The spatial extent of the neural response to an induced electric field has been previously calculated using the second spatial difference of the voltage distribution applied along the axon (Butson & McIntyre, 2005; 2006; Butson et al, 2007). Our conservative estimate of the VOCA model in the isotropic model underestimated these calculations. However, unlike previously published unvalidated theoretical analyses, we validated the predicted tractography of activated axonal bundles post-implantation using SAS.

Isotropic E-field modeling, as described here, was important as a first approximation for determining the maximal undistorted E-field density surrounding the active electrode contacts. Conductivity values of homogeneous white and grey matter used to calculate the electric field in this study were taken from published databases. Therefore, validation of these estimates was not performed with individual specificity. These values were determined based on a stimulation frequency of 200 Hz (Andreucetti et al, 2005; Gimsa et al, 2004). This stimulation frequency is typically used for mesial temporal epileptic sources during the RNS™ Pivotal Clinical Trial.

More sophisticated anisotropic modeling took into account tissue conductivity in a hetero-geneous tissue medium. However, a 3D VOCA could not be generated due to COMSOL software constraints placed on the significant data processing demand required. That is, COMSOL did not accommodate for parallel processing. Therefore, the software was incapable of engaging multiple CPU cores when manipulating a geometry composed of multiple rectangles, or voxels, in which each rectangle was defined by a tensor array. Specifically, 8100 tensor datasets were passed on to COMSOL by our MATLAB program. The anisotropic 2D model required about 10 days of continuous processing to include the electrode and its physical conductivity properties into the generated geometry. An additional 44 hours, 40 minutes, and 44 seconds were required to perform the E-field solution on a 64 bit dual processor 16 core workstation with 192 GB accessible RAM. Anisotropic modeling is obviously preferable since it takes into account tissue pathology at the resolution of a DTI voxel. In effect, DTI can be used to predict the electrical conductivities of local brain tissue based on the supposition that DTI eigenvalues and electrical conductivity have a linear relationship in the human brain (Astrom et al, 2012; Akhtari et al, 2006; Tuch et al, 2001). Such data can be validated *in vivo* in the operating room to provide accurate individual models of direct brain stimulation.

While the Poisson equation provides a spatial voltage solution, it does not account for the time dependence of the stimulus waveform or the capacitance of the electrode-tissue interface. Similar to the constant voltage circuit used by the Medtronic DBS IPG for movement disorders, the actual stimulus delivered to brain tissue by the constant current charging circuit of the RNS™ System neurostimulator may be modified by an interdependent tissue capacitance and impedance, which change slowly over time. An evolving capacitance is related to an encapsulation sheath surrounding the electrode lead (McIntyre et al, 2004; Butson & McIntyre, 2005; Miocinovic et a, 2006; Butson et al, 2006). We assumed a constant 500 Ohm electrode-tissue interface resistance without a capacitance. Therefore, a constant potential difference of 5 V peak-to-peak was also assumed.

The electric field lines determined in our model were used to estimate a threshold value to activate a critical volume of white matter surrounding the electrode contacts. The E-field of interest surrounding each active contact was assumed to be undistorted and spherical. The 220 mm^3 volume of a static electric field geometry used to estimate the VOCA surrounding each

electrode contact agreed with previous literature (McIntyre et al, 2004; Vasques et al, 2008). However, near-field regions at the cylindrical contact edges where the fringe electric field becomes complex were not considered in our calculations. Of interest, a neuron exposed to these fringe fields can experience both inward and outward transmembrane currents, therefore resulting in neuronal hyperpolarization or depolarization, respectively (McIntyre et al, 2004). An ability to account for these effects was beyond the voxel resolution of our DTI protocol.

Lastly, axon fibers oriented parallel to the active depth contacts were exposed to a larger voltage gradient and assumed to be preferentially activated in our model. An understanding of depth lead orientation is important for maximizing activation of surrounding white matter. Axons oriented predominantly in the direction of the voltage gradient are more likely to be activated, compared to axons oriented perpendicularly to the voltage gradient along isopotential lines (Rise, 2004).

The pre-implant modeled propagation map was validated post-implantation by utilizing SAS. Such a validation tool capitalizes on the coupling of blood flow changes with the metabolic demand placed on neuronal populations induced by electrical stimulation. Perfusion-related changes along with concordant clinical manifestations of direct cortical stimulation of mesial temporal white matter validate the presurgical cortical activation model. We have previously demonstrated discrete hypo-perfusion-related changes both at the site of stimulation and propagated at a distance (Rossi et al, 2008; Rossi et al, 2010). These findings are, in part, similar to previous reports of stimulation-related SPECT changes (Velasco et al, 2000). The underlying mechanisms explaining these changes are unknown. However, one hypothesis is that these local regions of transient hypoperfusion represent inhibitory activation, or suppressive communicating epileptic networks (Chkhenkeli et al, 2007).

Although limited to a single patient, the concordance of anticipated cortical activation targets with post-implant stimulation-related transient blood flow changes provide evidence that such electrode lead placement planning is feasible. These data further suggest that direct stimulation of white matter can be used to guide the spread of stimulation therapy to distant communicating neural targets. As a result, a greater extent of the epileptic circuit can be modulated with a minimal number of electrodes.

5. Use of COMSOL Multiphysics

COMSOL was used to obtain an E-field and a current density solution, applying a static electric potential when the electrical conductivity was known. This is illustrated by equations 1 and 2:

$$\vec{J} = \sigma \vec{E} \tag{1}$$

Where $\vec{J}$ is the current density, σ is the electrical conductivity of the material, and $\vec{E}$ is the electric field.

$$\vec{E} = \nabla V \tag{2}$$

Where V is the applied electric potential, and ∇ is the differential operator.

In the isotropic model, the conductivity σ was stated by segmenting three brain tissue compartments (white matter, grey matter and CSF). Thus, three different domains were generated with three different conductivities.

Whereas, in the anisotropic model, σ was obtained for each modeled voxel from the water diffusion second rank symmetric tensors acquired from DTI.

$$\boldsymbol{D} = \begin{bmatrix} Dxx & Dxy & Dxz \\ Dxy & Dyy & Dyz \\ Dxz & Dyz & Dzz \end{bmatrix} \tag{3}$$

These diffusion tensors were converted into conductivity tensors using a linear relationship of the tensor matrices' eigenvalues.

$$\boldsymbol{\sigma} = \left(\frac{\sigma_e}{d_e}\right)\boldsymbol{D} \tag{4}$$

Where $\left(\frac{\sigma_e}{d_e}\right)$ is a numeric constant with value of $0.736\ \frac{S(s)}{mm^3}$ (Tuch et al, 2001).

6. Figures

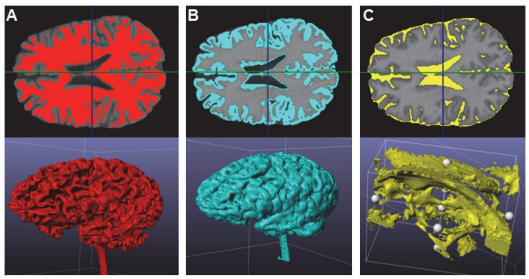

Figure 1. Segmentation of the subject's high-resolution SGPR MRI dataset (124 contiguous slices, voxel resolution: 0.859 mm^3) was performed in the Simpleware Software Suite to create a FEM mesh prior to importing into COMSOL Multiphysics v4.3b for calculating the biophysics of stimulation. **(A)** White matter, **(B)** grey matter, and **(C)** CSF compartments are shown.

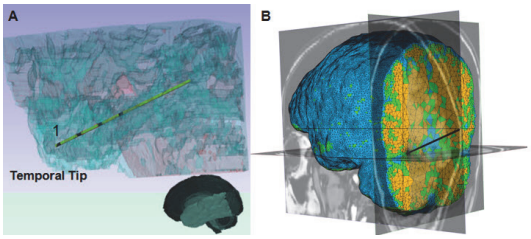

FIGURE 2. (A) A CAD rendering of the depth electrode model consisted of four conductive cylinders (1.27 mm diameter x 0.2 mm height) separated by insulators (10 mm between cylinder midpoints). Using the Simpleware +CAD module, this electrode model was positioned longitudinally (from occipital to frontal) in epileptic temporal lobe white matter within 4-5 mm of the grey-white matter interface. **(B)** A variable mesh density was employed, with a maximum edge length of 0.25 mm lying within a 40 mm radius surrounding each electrode contact. The variable mesh transitioned linearly outward to a maximum edge length of 5 mm.

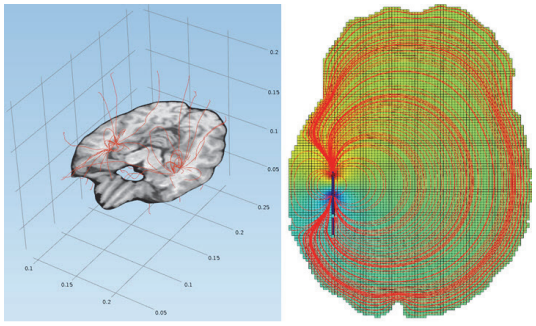

FIGURE 3. The 3D and 2D isotropic models representing the uniform E-field are shown. The platinum/iridium electrode contact conductivity was set to $15x10^6$ S/m. White matter was represented as a homogeneous and isotropic tissue medium where, conductivity=0.15 S/m. Adjacent isotropic grey matter conductivity was set to 0.06 S/m, and CSF = 1.79 S/m. The planar slice is neurologically oriented.

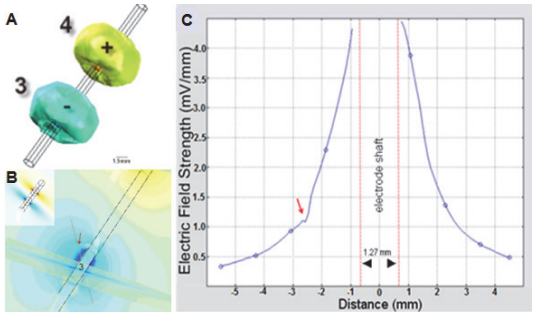

FIGURE 4. (A) The radial strength of the generally symmetric and spherical electric field was modeled as isosurfaces **(B).** A radius of 3.75 mm from shaft center (midline between parallel red dotted lines) was assumed to influence axons encompassed by the maximal magnitude of the electric field **(C)**. Sudden transient drops of the electric field (red arrow in **B & C**) are seen near the fringes of the electric field surrounding the active cylindrical contacts.

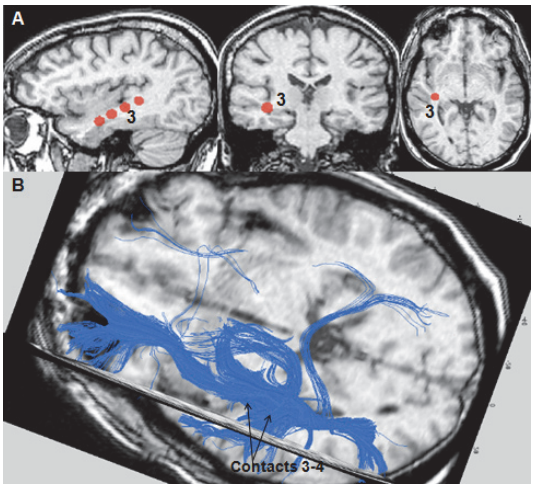

FIGURE 5. (A) The VOCA spheres (orange) generated by our isotropic modeling were used as regions of interest for positioning in the left temporal white matter overlapping the parahippocampal whjite matter. **(B)** The pre-implant tractography model is shown. This depth lead planning model represents the anticipated extent of white matter tracts influenced by stimulation. The tractography model was generated using deterministic tracking algorithm from a continuous tensor field of the tensor elements (MR VISTA). Images are neurologically oriented.

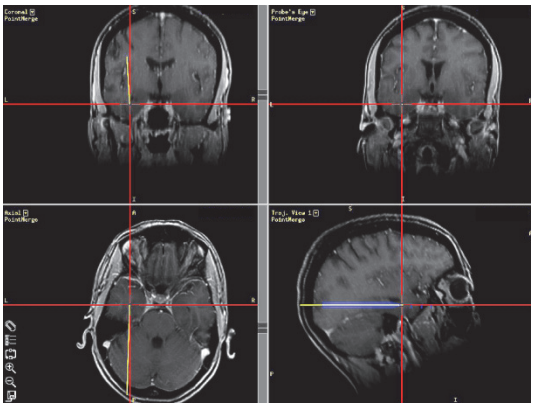

FIGURE 6. Stereotactic implantation of the depth lead is shown in paramesial white matter of the left temporal lobe guided by our pre-implantation isotropic depth lead planning model. The right paramesial temporal region was also implanted similarly. An occipital approach was used for both 4-contact depth leads employing an intraoperative Stealth^{TM} MRI navigational system (Medtronic, Inc). Images are neurologically oriented.

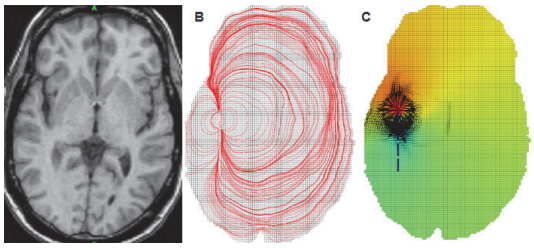

FIGURE 7. A 2D anisotropic conductivity model of the E-field **(B)** and current density maps **(C)** are shown. The anisotropic associated E-field and current densities followed anatomical boundaries not apparent in the isotropic conductivity model. DTI voxel resolution: 1.95 x 1.95 x 3 mm^3. Images are neurologically oriented.

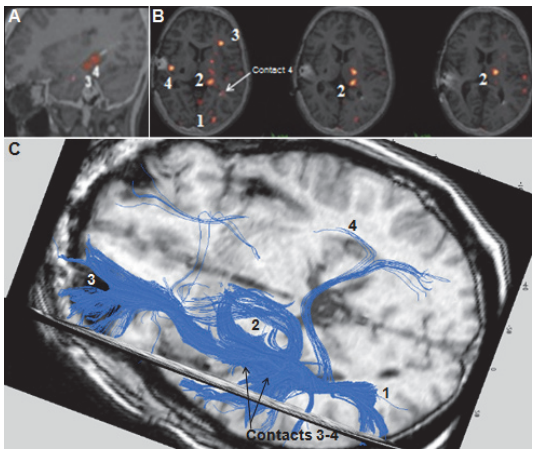

FIGURE 8. (A) The VOCA ROI 3.75 mm radius seeds surrounded the implanted depth electrode contacts seen on CT co-registered to MRI. **(B)** The SAS regions of transient hypoperfusion co-registered to MRI are shown (slices are radiologically oriented). This technique validated the isotropic VOCA modeling of pre-implant electrode planning in the left temporal electrode lead. Contacts 3 & 4 were stimulated without causing a seizure (after-discharge). The grey matter regions of transient hypoperfusion included: 1) ipsilateral (left) occipital lobe, 2) ipsilateral thalamus, 3) ipsilateral (left) basal frontopolar region, and 4) the contralateral posterior superior temporal gyrus. **(C)** The pre-implant generated tractography modeled white matte tracts are shown connecting the SAS regions. As importantly, the tractography terminate near or within regions concordant with the SAS study.

7. Conclusions

We have proposed a computationally-intensive system that facilitated planning of implantation sites, electrode orientation, and basic stimulation parameters for depth electrodes in juxtacortical mesial temporal white matter for this investigational direct neuromodulation technology. Our pre-implantation isotropic model simulation was validated post-implantation as measured by our SAS technique. However, anisotropic modeling for optimizing electrode placement planning will likely improve the probability of modulating the maximal extent of a bilateral temporal lobe epileptic network with a minimum of depth electrode contacts. Development of this strategy using 3D anisotropic modeling of predicted stimulation pathways will provide a better understanding and clarity of individual differences seen with direct cortical stimulation therapy of white matter pathways. Such a brain-device interface planning system will not only predict influencing distant epileptic neural tissue using direct neurostimulation, but also enhance the ability to strategically interface neural prostheses with extensive neural networks.

8. References

1. Akhtari M, Salamon N, Duncan R, Fried I, Mathern GW. Electrical conductivites of the freshly excised cerebral cortex in epilepsy surgery patients: Correlation with pathology, seizure duration, and diffusion tensor imaging. **Brain Topography 18:**281-290 (2006).

2. Andreuccetti D, Fossi R, Petrucci C. Dielectric properties of body tissue Italian Research Council, Institute for Applied Physics, Florence, Italy. http://niremf.ifac.cnr.it/tissprop (2005).

3. Astrom M, Johansson JD, Hariz MI, Eriksson O, Wardell K. The effect of cystic cavities on deep brain stimulation in the basal ganglia: A simulation-based study. **J Neurol Eng 3:**132-138 (2006).

4. Astrom M, Lemaire JJ, Wardell K. Influence of heterogeneous and anisotropic tissue conductivity on electric field distribution in deep brain stimulation. **Medical and Biological Eng Comp 50**(1):23-32 (2012).

5. Benabid AL, Chabardes S, Mitrofanis J, Pollak P. Deep brain stimulation of the subthalamic nucleus for the treatment of Parkinson's disease. **Lancet Neurology 8:**67-81 (2009).

6. Beurruer C, Bioulac B, Audin J, Hammond C. High-frequency stimulation produces a transient blockade of voltage-gated currents in subthalamic neurons. **J Neurophysiol 85:**1351-1356 (2001).

7. Boon P, Vonck K, De Herdt V, Van Dycke A, Goethals M, Goossens L, Van zandijcke M, De SmeDt T, Dewaele I, Achten R, Wadman W, Dewaele F, Caemaert J, Van Roost D. Deep brain stimulation in patients with refractory temporal lobe epilepsy. **Epilepsia 48:**1551-1560 (2007).

8. Butson CR, McIntyre CC. Tissue and electrode capacitance reduce neural activation volumes during deep brain stimulation. **Clin Neurophys 116:**2490-2500 (2005).

9. Butson CR, McIntyre CC. Role of electrode design on the volume of tissue activated during deep brain stimulation. **J Neurol Eng 3:1-8** (2006)**.**

10. Butson CR, Cooper SE, Henderson JM, McIntyre CC. Patient-specific analysis of the volume of tissue activate during deep brain stimulation. **NeuroImage 34:**661-670 (2007).

11. Chkhenkeli SA, Towle VL, Lortkipanidze GS, Spire J-P, Bregvadze ES, Hunter JD, Kohrman M, Frim DM. Mutually suppressive interrelations of symmetric epileptic foci in bitemporal epilepsy and their inhibitory stimulation. **Clin Neurol Neurosurg 109:**7-22 (2007).

12. Dale AM, Fischl B, Sereno MI. Cortical surface-based analysis. I. Segmentation and surface reconstruction. **Neuroimage 9:**179-194 (1999).

13. de Crespigny, AJ, Moseley, ME. Eddy current induced image warping in diffusion weighted EPI. In: **Abstr of the Int Soc of MR in**

Med; Sydney, Australia. Abstr 2661 (1998).

14. Diehl B, Symms MR, Boulby PA, Salmenpera T, Wheeler-Kingshott CAM, Barker GJ, Duncan JS. Postictal diffusion tensor imaging. **Epilepsy Res. 65:**137-146 (2005).

15. Dostrovsky JO, Levy R, Wu JP, Hutchison WD, Tasker RR, Lozano AM. Microstimulation-induced inhibition of neuronal firing in human globus pallidus**. J Neurophysiol 84:**570-574 (2000).

16. Durand DM, Bikson M. Control of neuronal activity by electric fields: in vitro models of epilepsy. In: Deep Brain Stimulation and Epilepsy. (Ed: Luders, HO). Martin Dunitz, London & New York. pp 67-86 (2004).

17 .Fisher R, Salanova V, Witt T, Worth R, Henry T, Gross R, Oomen K, Osorio I, Nazzaro J, Labar D, Kaplitt M, Sperling M, Sandock E, Neal J, Handforth A, Stern J, DeSalles A, Chung S, Shetter A, Bergen D, Bakay R, Henderson J, French J, Baltuch G, Rosenfeld W, Youkilis A, Marks W, Garcia P, Barbaro N, Fountain N, Bazil C, Goodman R, McKhann G, Krishnamurthy B, Papavassiliou S, Epstein C, Pollard J, Tonder L, Grebin J, Coffey R, Graves N. Electrical stimulation of the anterior nucleus of thalamus for treatment of refractory epilepsy. **Epilepsia 51:**899-908 (2010).

18. Fukuda M, Mentis MJ, Ma Y, Moeller JR, Dhawan V, Antonini A, Lang AE, Lozano AM, Hammerstad J, Lyons K, Koller WC, Eidelberg D. Networks mediating the clinical effects of pallidal brain stimulation for Parkinson's disease: A PET study of resting-state glucose metabolism. **Brain 124:**2105-2118 (2001).

19. Gimsa J, Habel B, Schreiber U, van Rienen U, Strauss U, Gimsa U. Choosing electrodes for deep brain stimulation experiments-electrochemical considerations. **J Neurosci Methods 142:**251-265 (2004).

20. Hodaie M, Wennberg RA, Dostrovsky JO, Lozano AM. Chronic anterior thalamus stimulation for intractable epilepsy. **Epilepsia 43:**603-608 (2002).

21. Keller A, Arissian K, Asanuma H. Synaptic proliferation in the motor cortex of adult cats after thalamic stimulation. **J Neurophysiol 68:**295-308 (1992).

22. Kiss ZHT, Doig-Beyaert K, Eliasziw M, Tsui J, Haffenden A, Suchowersky O. The Canadian multicentre study of deep brain stimulation for cervical dystonia. **Brain 130:**2879-2886 (2007).

23. Lavenex P, Banta Lavenex P, Amaral DG. Postnatal development of the primate hippocampal formation. **Dev Neurosci 29:**179-192 (2007).

24. Lesser, RP, Kim SH, Beyderman L, et al. Brief bursts of pulse stimulation terminate afterdischarges caused by cortical stimulation. **Neurology 53:**2073-2081 (1999).

25. Luders J, Najm I, Luders HO. Brain stimulation and epilepsy: basic overview and novel approaches. In: Deep Brain Stimulation and Epilepsy. (Ed: Luders, HO). Martin Dunitz, London & New York. pp 3-17 (2004).

26. McIntyre DC, Goddard GV. Transfer, interference and spontaneous recovery of convulsions kindled from the rat amygdale. **Electroencephalogr Clin Neurophysiol 35:**533-543 (1973).

27. McIntyre CC, Grill WM. Finite element analysis of the current-density and electric field generated by metal microelectrodes. **Ann Biomed Eng 29:**227-235 (2001).

28. Mcintyre CC, Mori S, Sherman DL, Thakor NV, Vitek JL. Electric field and stimulating influence generated by deep brain stimulation of the subthalamic nucleus. **Clin Neurophys 115:**589-595 (2004).

29. Miocinovic S, Parent M, Butson CR, Hahn PJ, Russo GS, Vitek JL, McIntyre CC. Computational analysis of subthalamic nucleus and lenticular fasciculus activation during therapeutic deep brain stimulation. **J Neurophys 96:**1569-1580 (2006).

30. Montgomery EB, Baker KB. Mechanisms of deep brain stimulation and future technical developments. **Neurol Res 22:**259-266 (2000).

31. Morrell, MJ, Hirsch, LJ, Bergey, G, Barkley, G, Wharen, R, Murro, A, Fisch, B, Rossi, MA, Labar, D, Duckrow, R, Sirven, JI, Drazkowski, J, Worrell, GA. Long-term safety and efficacy of the RNS system in adults with medically-intractable partial onset seizures. **Epilepsia 49(s7):**480 (2008).

32. Morrell MJ, Hirsch LJ, Bergey G, Barkley G, Wharen R, Murro A, Fisch B, Rossi MA, Labar D, Duckrow R, Sirven JI, Drazkowski J, Worrell GA, Gwinn RP. Results of a multicenter double blinded randomized controlled pivotal investigation of the RNS™ system for treatment of intractable partial epilepsy in adults. **AES Abstr B09** (Platform) (2009).

33. Obeso JA, Olanow CW, Rodriguez-Oroz MC, Krack P, Kumar R, Lang AE. Deep-brain stimulation of the subthalamic nucleus or the pars interna of the globus pallidus in Parkinson's disease. **N Engl J Med 345:**956-963 (2001).

34. Prichard JW, Zhong J, Petroff OA, Gore JC. Diffusion-weighted NMR imaging changes caused by electrical activation of the brain. **NMR Biomed 8:**359-364 (1995).
Rise MT (2004) Brain stimulation and epilepsy: electrical stimulus characteristics. In: Deep Brain Stimulation and Epilepsy. (Ed: Luders, HO). Martin Dunitz, London & New York. pp 45-54.

35. Rossi MA, Hoeppner TJ, Byrne RW, Greene D, Kanner AM, Stoub T, Stein MA, Balabanov A, Bergen D, Smith MC. Subtracted activated SPECT validates depth lead placement in white matter for responsive neurostimulation therapy in refractory partial-onset epilepsy. **Epilepsia 49(Suppl 7)** abstr 3.102 (2008).

36. Rossi MA, Krug K. Improved localization of extratemporal ictal onset-associated blood flow changes using a 72-detector scanning focused collimator SPECT system. **AES Abstr 1.182** (2012).

37. Rossi MA Stebbins G, Murphy C, Greene D, Brinker S, Sarcu D, Tenharmsel A, Stoub T, Stein MA, et al. Predicting white matter targets for direct neurostimulation therapy. **Epilepsy Res 91**(2-3):176-186 (2010).

38. Salmenpera TM, Symms MR, Boulby PA, Barker GJ, Duncan JS. Postictal diffusion weighted imaging. **Epilepsy Res 70:**133-143 (2006).

39. Tellez-Zenteno JF, McLachlan RS, Parrent A, Kubu CM, Weibe S. Hippocampal electrical stimulation in mesial temporal lobe epilepsy. **Neurology 66:**1490-1494 (2006).

40. Tuch TS, Wedeen VJ, Dale AM, George JS, Belliveau JW. Conductivity tensor imaging of the human brain using diffusion tensor MRI**. Proc Natl Acad Sci 98:**11697-11701 (2001).

41. Urbano FJ, Leznik E, Llinas RR. Cortical activation patterns evoked by afferent axons stimuli at different frequencies: an in vivo voltage-sensitive dye imaging study. **Thalamus Rel Syst 1:**371-378 (2002).

42. VanLandingham KE, Lothman EW. Self-sustaining limbic status epilepticus. II. Role of hippocampal commissures in metabolic responses. **Neurology 41:**1950-1957 (1991).

43. Vasques X, Cif L, Hess O, Gavarini S, Mennessier G, Coubes P. Stereotactic model of the electrical distribution within the internal globus pallidus during deep brain stimulation. **J Comput Neurosci** DOI 10.1007/s10827-008-0101-y (2008).

44. Velasco M, Velasco F, Velasco AL, Boleaga B, Jimenez F, Brito F, Marquez I. Subacute electrical stimulation of the hippocampus blocks intractable temporal lobe seizures and paroxysmal EEG activities. **Epilepsia 41:**158-169 (2000).

45. Velasco M, Velasco F, Velasco AL, Menez D, Rocha L. Electrical stimulation for epilepsy: Stimulation of hippocampal foci. **Stereotact Funct Neurosurg 77:**223-227 (2001).

46. Velasco M, Velasco F, Brito F, Velasco AL, Nguyen JP, Marquez I, Boleaga B, Keravel Y. Motor cortex stimulation in the treatment of deafferantation pain. I. Localization of the motor cortex. **Stereotact Funct Neurosurg 79:**146-167 (2002).

47. Vidailhet M, Vercueil L, Houeto JL, Krystkowiak P, Benabid AL, Cornu P,

Lagrangem C, Tezenas du Montcel S, Dormont D, Grand S, Blond S, Detante O, Pillon B, Ardouin C, Agid Y, Destee A, Pollak P. Bilateral deep-brain stimulation of the globus pallidus in primary generalized dystonia. **N Engl J Med 352:**459-467 (2005).

48. Vonck K, Boon P, Achten E, DeReuck J, Caemaert J. Long-term amygdalo-hippocampal stimulation for refractory temporal lobe epilepsy. **Ann Neurol 52:**556-565 (2002).

49. Yogarajah M, Duncan JS. Diffusion-based magnetic resonance imaging and tractography in epilepsy. Epilepsia 49:189-200 (2008).

50. Zhong J, Petroff OA, Pleban LA, Gore JC, Prichard JW. Reversible, reproducible reduction of brain water apparent diffusion coefficient by cortical electroshocks. **Magn Reson Med 37:**1-6 (1997).

51. Zumsteg D, Lozano AM, Wennberg RA. Mesial temporal inhibition in a patient with deep brain stimulation of the anterior thalamus for epilepsy. **Epilepsia 47:**1958-1962 (2006).

9. Acknowledgements

Support from Simpleware, LTD, NeuroLogica Corp, Inc as well as RUMC departmental and institutional resources are gratefully acknowledged.

10. Disclosure of Conflicts of Interest

All authors have no professional or financial affiliations that might be perceived as having biased the presentation. The authors have provided full disclosure of any conflict(s) of interest and have no conflicts of interest to disclose.